Energy & Environmental Science

Unique Interfacial Thermodynamics of Few-Layer 2D MoS2 for (Photo)electrochemical Catalysis

Journal:	*Energy & Environmental Science*
Manuscript ID	EE-ART-02-2019-000513.R1
Article Type:	Paper
Date Submitted by the Author:	01-Apr-2019
Complete List of Authors:	Carroll, Gerard; National Renewable Energy Laboratory, Chemistry and Nanoscience Zhang, Hanyu; National Renewable Energy Laboratory, Chemistry and Nanoscience Dunklin, Jeremy; National Renewable Energy Laboratory, Chemistry and Nanoscience miller, elisa; National Renewable Energy Laboratory, Chemistry and Nanoscience Neale, Nathan; National Renewable Energy Laboratory, Chemistry and Nanoscience van de Lagemaat, Jao; National Renewable Energy Laboratory, Chemistry and Nanoscience

Carroll et al.
April 1, 2019

Unique Interfacial Thermodynamics of Few-Layer 2D MoS_2 for (Photo)electrochemical Catalysis

G. Michael Carroll,* Hanyu Zhang, Jeremy R. Dunklin, Elisa M. Miller, Nathan R. Neale and Jao van de Lagemaat*
Chemistry and Nanoscience Center, National Renewable Energy Laboratory, 15013 Denver West Parkway, Golden, Colorado 80401, United States
Email: Mike.Carroll@nrel.gov, Jao.Vandelagemaat@nrel.gov

Broader Context. Heterogeneous semiconductor (photo)electrocatalysis is an important avenue of research for adapting commodity chemical supply to a renewable energy-based global economy. The fundamental thermodynamics that govern electron transfer processes are generally understood within the framework pioneered by Gerischer and Marcus. Their principals have guided the understanding and predictive power of materials design for bulk-semiconductor heterogeneous (photo)electrocatalysis. However, the discovery of new materials, such as van der Waals bound 2D transition metal dichalcogenides, display electronic characteristics unlike those found in bulk semiconductors and may lead to the next generation of (photo)electrocatalysts. Adaptation of the fundamental electrochemical principles that guide catalyst design is required to utilize these materials in a heterogenous catalyst configuration. Here, we investigate the interfacial thermodynamic properties of few-layer molybdenum disulfide (MoS_2) thin films through *in situ* spectroelectrochemical measurements. We find that the classical description of the free-energy of charge transfer (ΔG_{CT}) at the semiconductor interface does not capture the reality of MoS_2 and discuss the implications of such effects for heterogeneous (photo)electrocatalysis.

Abstract. The electronic structure of few-layer MoS_2 is studied by *in-situ* and *operando* spectroelectrochemistry in conditions relevant to its use as an electrocatalyst. We show that electron injection into the conduction band is coupled with a redshift of the exciton resonance, the magnitude of which depends on the number of vertical MoS_2 layers. In addition, the applied electric field/electronic doping imparts uniaxial tensile strain evidenced by broadening Raman signals, indicating that under conditions of electrocatalysis, the system is structurally different from equilibrium. We demonstrate that field/carrier induced changes to the electronic structure of MoS_2 alter the band edge positions which changes the fundamental thermodynamic driving force for charge transfer. This property is a function of the applied potential, an effect unique to 2D semiconductors. The dynamic band edge potentials change the relevant interfacial energetics for charge transfer and has strong implications for the mechanistic understanding of (photo)catalytic fuel-forming reactions using two-dimensional systems.

Introduction

Electrochemical and photoelectrochemical catalysis to generate value added chemicals from abundant natural resources is a central challenge to realize a renewable-based electrified economy. Tailoring thermodynamic driving forces and kinetic pathways for heterogeneous charge transfer processes at the surface of semiconductors is a strategy to improve the efficiency of catalysis. Generally, mechanisms to shift interface energies are chemical or ionic modification of the semiconductor interfaces such as appending molecules to impart electric dipoles,[1, 2] engineering

defect states,[3, 4] passivating native interface states to alleviate Fermi-level (E_F) pinning[5] or pH modulation to tune Nernstian-behaving electrodes.[6] Lattice strain induced by mechanical stress can also improve electrode kinetics through modified surface energies.[7, 8] Finding and characterizing new ways to tune interfacial charge transfer is indeed a fruitful avenue for advancing heterogeneous catalysis.

Two-dimensional transition metal dichalcogenides (TMDCs) in either monolayer or van der Waals (vdW)-bound, few layer form are promising potential candidates for electrocatalysis in a variety of chemical transformations; in particular, the hydrogen evolution reaction (HER).[9-13] The exchange current (j_0) (a measure of the catalytic activity spanning ~10 orders of magnitude) for the 1T-phase of MoS_2, for example, is $j_0 = 7.9 \times 10^{-6}$ A/cm^2 only slightly less than platinum [111] which is $j_0 = 4.5\times 10^{-4}$ A/cm^2.[10] These MoS_2 efficiencies can be further optimized with defect engineering.[14, 15] The 2H-phase of TMDCs is semiconducting and strongly absorbs light in the visible spectrum making possible direct photoelectrocatalysis in bulk,[16, 17] few,[18, 19] and monolayer limits.[9, 20-22] Under standard electrochemical and photoelectrochemical operating conditions, however, 2D TMDCs display unconventional characteristics. For example, the interfacial charge transfer rate constants of molybdenum disulfide (MoS_2) under photoelectrochemical conditions depend linearly (or super-linearly) on light intensity.[20] This is in contrast to the expected semiconductor electrode kinetics where the charge transfer rate constant is unchanged with light and electrochemical bias.[23] Heterogeneous charge transfer occurs at a fixed energy through the semiconductor band edge which leads to a light-bias independent charge transfer rate constant. In addition, it has been observed that charge transfer rate constants and catalytic overpotentials for H_2 evolution on TMDCs depend on the number of vdW-bound layers.[20, 21, 24] These observations have been explained by anisotropic carrier diffusion profiles, but the atypical catalytic behavior of these semiconductors also may be related to their unique physical properties under applied electric fields.

The electronic, optoelectronic and structural properties of mono- and few-layer TMDCs under applied electric fields are also interesting.[25] For example, when electrons are injected into monolayer 2H-MoS_2 conduction band under applied bias, and the exciton binding energies are reduced by hundreds of meV through phase space filling and carrier screening,[26-28] but giant band gap renormalization effects[27, 29] oppose the reduced exciton binding energies to a similar magnitude such that the exciton resonance energies are virtually unchanged. Spectroscopically resolvable trions are also formed.[30, 31] Structurally, monolayer and odd layer MoS_2 are piezoelectrically active due to the lack of centro-symmetry in the crystal structure.[32] In the few-layer limit, electric fields themselves modulate both the band gap[33-38] as well as induce electromechanical strain.[39, 40] These unusual physical properties present new and interesting possibilities for (photo)electrocatalysis, but a contextualization of the relevant differences between 2D materials and typical semiconductor electrodes is first required.

Here, we employ spectroelectrochemistry in UV/vis and Raman configurations as an *in-situ* probe to understand the role of electric fields and electronic doping on 2D, few layer 2H-MoS_2 thin film electrodes. By electrochemically modulating the MoS_2 Fermi level (E_F) into an energetic region outside of the band gap, we reversibly dope MoS_2 with delocalized carriers (Figure 1a). The resulting many-body effects display characteristic spectroscopic signatures that can be studied to understand the relevant changes to the electronic structure and interfacial thermodynamics.[41, 42] We find that both electron injection and band gap reduction are achieved under applied bias where the magnitude of the band gap energy shift as well as carrier density depend on the MoS_2 dimensions. *In-situ* Raman measurements both confirm the presence of charge carriers and present

evidence for field-/carrier-induced lattice strain. We analyze the spectroscopic changes and demonstrate that the traditional carrier density dependence on applied potential for semiconductors is not present. Rather, an additional screening factor—unique to 2D semiconductors—dictates the voltage-dependent carrier density. We further discuss the implications of such a property within the context of (photo)electrochemical catalysis. Finally, we demonstrate that these processes occur under bulk electrolytic HER conditions by performing *operando* spectroelectrochemical measurements.

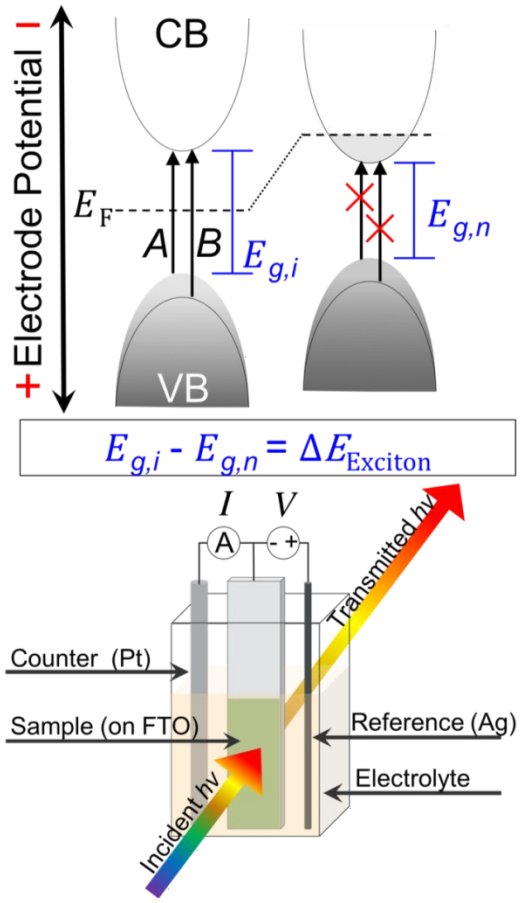

Figure 1. Schematic illustrations of MoS_2 capacitive conduction band filling under electrochemical bias (top) and the spectroelectrochemical setup used to probe MoS_2 potential-dependent spectroscopic properties (bottom). Under intrinsic conditions, the Fermi level is located within the band gap, but as the electrode potential is swept cathodically electrons are reversibly injected into the MoS_2 conduction band. Under these conditions, the lowest energy electronic transitions are bleached as a result of Pauli blocking and, at the same time, the bandgap energy decreases due to renormalization effects ($\Delta E_{Exciton}$). For simplicity, only the direct electronic transitions are shown in the schematic.

Results and Analysis

The evolution of the MoS_2 band structure with decreasing sheet number is well understood.[43-46] Upon exfoliation of vdW-bound 2H-MoS_2, the lowest energy electronic excitation

evolves from an indirect Γ to Λ transition in the bulk to a direct K to K transition in the monolayer limit.[44] The valence band at the K point is split through spin-orbit interactions giving rise to two excitonic features, A and B. UV/vis absorption measurements of these excitonic features is used to probe the carrier density under varying potentiostatic bias.

Thin films of MoS_2 flakes in the 2H-phase with varying average lateral ($< L >$) and average layer-number thickness ($< N >$) dimensions are deposited onto clean fluorine-doped tin oxide (FTO) electrodes. The average flake dimensions are determined optically, and we estimate the size distribution (one standard deviation from the mean) as ~10% of the mean value of $< N >$ or $< L >$.[47, 48] The MoS_2 thinfilm electrodes display an optical density of ~0.1 at the A-exciton (lowest-energy) peak. The prepared films are submerged in dry, anaerobic acetonitrile with 0.1 M tetrabutylammonium hexafluorophosphate ($[Bu_4N][PF_6]$) as a supporting electrolyte in a standard three electrode configuration (Pt counter and Ag quasi-reference electrodes). The MoS_2 E_F is controlled with potentiostatic bias in 0.1 V intervals, where absorption spectra (transmission) are collected at each bias. A schematic representation of the experimental setup used in this study is shown in Figure 1, bottom. Further experimental details are presented in the supporting information.

Figure 2a plots the absorption spectra of $< N >$ = 3 monolayer (ML), $< L >$ = 150 nm 2H-MoS_2 under potentiostatic bias between +2 and –2 V. The UV/vis absorption spectrum at the open-circuit potential (V_{oc} = 0.1 V *vs* Ag) contains two well-defined features at 1.87 and 2.05 eV attributed to the spin-orbit split A and B excitons. As the potential is swept positive away from V_{oc}, the absorption peak for both the A and B excitons gains intensity and shifts to higher energies (blue-shifts) until ~1.5 V. Intensity loss and red-shifts are observed at potentials more positive than 1.5 V. Conversely, sweeping to negative potentials from V_{oc} results in continuous red-shifting of the exciton peaks as well as a decrease in the absorption intensity until the end of the voltammetric window at –2 V.

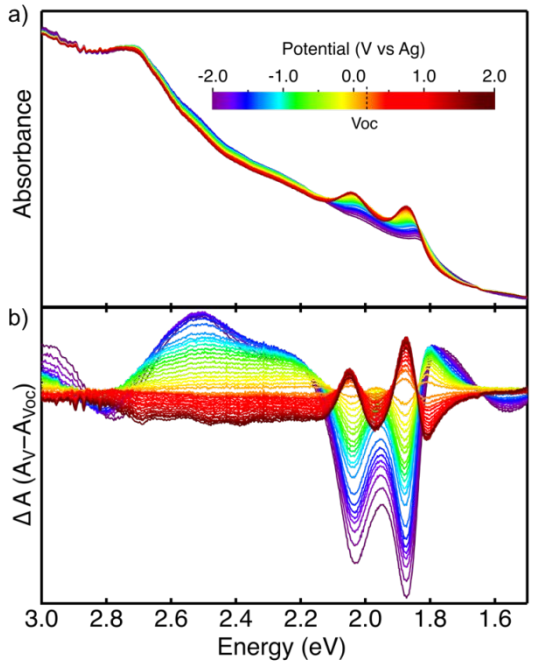

Figure 2. (a) Electronic absorption spectra of $< N >$ = 3 ML MoS_2 deposited on FTO submerged in 0.1 M $[Bu_4N][PF_6]$ acetonitrile electrolyte. The colors correspond to the applied potential at which the spectrum is collected, indicated by the color bar. **(b)** Difference spectra from Figure 2a between the absorption spectrum

of MoS_2 at a given potential (A_V) and the absorption spectrum at the open circuit potential (A_{Voc}). The open-circuit potential is found to be 0.1 V *vs* Ag.

Figure 2b plots the difference spectra between MoS_2 absorption at a given applied potential and the absorption at V_{oc} ($A_V - A_{Voc}$). Under positive bias, the A and B exciton features display an induced absorption and blue-shift until a maximum is reached (~1.5 V) indicating that MoS_2 on FTO is *n*-type under V_{oc} conditions, consistent with prior reports.[26, 49] With positive bias, we deplete the conduction band of delocalized charge carriers, as indicated by the maximal absorption, providing a clear spectroscopic picture of intrinsic MoS_2. As the potential is swept in the negative direction from V_{oc}, the A and B exciton absorption intensity decreases and red-shifts as indicated by the derivative shape of the spectrum. The continuous excitonic bleach indicates increasing electron density to the MoS_2 conduction band with negative bias. We note that despite only populating the conduction band with electrons, the features in these spectra closely resemble those obtained from transient absorption measurements, where an excitonic bleach is coupled with a redshift.[50-52] For samples with $< N > \geq 2$, we also observe an absorption bleach associated with indirect $\Gamma \rightarrow \Lambda$ transition at ~1.5 eV (Figure S3). These are clear spectral signatures of both Pauli blocking and band gap renormalization as a result of an increasing population of conduction band electrons. We observe similar spectral features for the related 2D material tungsten disulfide, (Figure S4) suggesting that these properties are general to TMDCs.

To understand the spectral changes in more detail, the A and B excitonic features are deconvoluted from the absorption spectrum by fitting the spectra with three Gaussian functions. Two peaks account for the A and B excitonic absorption and the third for the indirect band gap absorption and scattering. The absorption spectra as well as the fits are presented for three different applied potentials (1.9, 0.0, and −1.5 V) in Figure 3a. From Figure 3a, the fitting procedure provides a satisfactory approximation of the experimental spectra. The fitting envelope (red line) results in residual values less than 1% of the absorption spectra (black dashed line) for any given wavelength at all potentials. Comparing the A and B exciton Gaussian fits across the three different potentials shown, the height decreases and peak positions red-shift for both exciton peaks with negative bias. The A exciton width was found to be nearly constant across all potentials (Figure S5) and therefore was held constant during the fitting procedure. The constant A exciton width indicates that the electric field is homogeneous across the MoS_2 layers. If, for example, the field is screened non-uniformly, the observed red-shifts would be unequal and, consequently, the exciton peak would appear broadened. Additionally, we do not observe a resolvable shoulder at the low energy edge of the A exciton corresponding to negative trion absorption.[31] The absence of trion absorption in multilayered MoS_2 spectra could reflect increased dielectric screening relative to the monolayer limit.

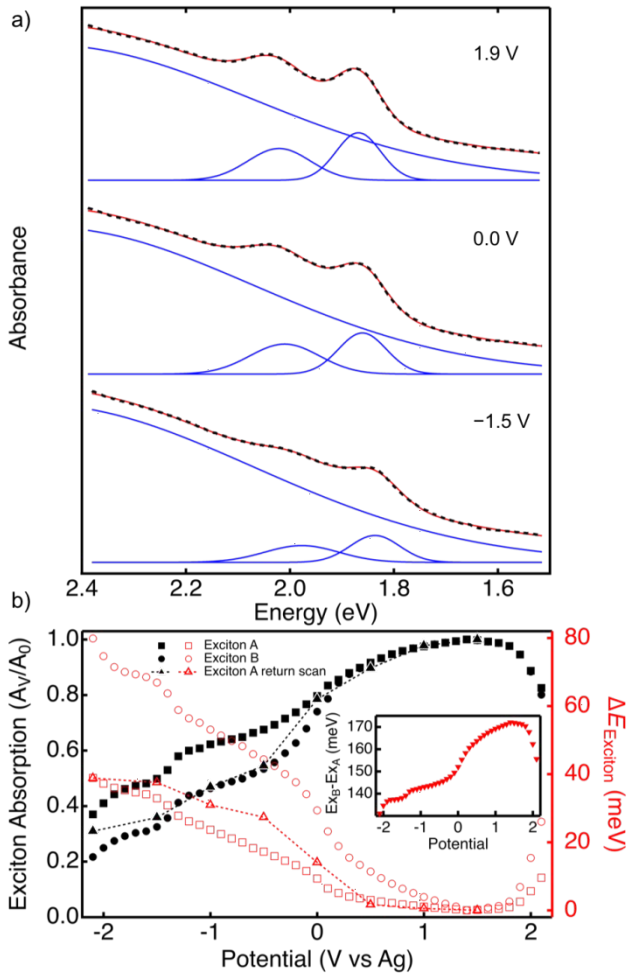

Figure 3. (a) Multiple Gaussian fits (blue) of absorption spectra (black dashed) of $<N_{avg}>$ = 3 ML MoS_2 at 1.9, 0.0, and –1.5 V *vs* Ag in 0.1 M $[Bu_4N][PF_6]$ acetonitrile electrolyte. The Gaussian envelope is shown in red. All spectra are fit with three Gaussians where the position and height are allowed to float during fitting. The width is held constant across all spectra for the A exciton. Panel **(b)** plots the normalized Gaussian peak height, A_V/A_0, (black, closed shapes) and the peak position shift, $\Delta E_{Exciton}$, (red, open shapes) of exciton A (squares) and exciton B (circles) as a function of the applied potential. Here, $A_V/A_0 = 1$ when the potential at which the absorption intensity is the highest, and $\Delta E_{Exciton}$ is the difference in energy (meV) between the absorption peak energy at the maximum ($A_V/A_0 = 1$) and at a given applied potential. Positive values of $\Delta E_{exciton}$ indicate a red (low energy) shift. Reverse direction scans of $\Delta E_{Exciton}$ (open triangles, dotted line) and A_V/A_0 (closed triangles, dotted line) also are shown. The inset shows the difference in energy between the A and B excitons.

In Figure 3b, we plot both the relative exciton absorption peak heights (A_V/A_0) and exciton peak energy shifts ($\Delta E_{Exciton} = E_0 - E_{Vapp}$) as a function of the applied potential for the A and B exciton features. A_0 is the maximum absorption measured, and A_V is the absorption at a given potential. A_V/A_0 displays a maximum at 1.5 V and decreases with either positive or negative bias (i.e., $A_V = A_0$ at $V_{App} = 1.5$ V). These data are the average of three different MoS_2 electrodes of the same colloidal source material. The uncertainty associated with these measurements can be found in the supporting information (Figure S6). At ~1 V, both A_V/A_0 and $\Delta E_{Exciton}$ begin continuous bleach and shift with increasingly negative bias until the end of the voltammetric window at –2.1 V, where A_V/A_0 for the A and B excitons are 0.38 and 0.2 and $\Delta E_{Exciton}$ is 38 meV and 80 meV,

respectively. At ~1 V and ~0.2 V, $\Delta E_{\text{Exciton}}$ and A_V/A_0 diverge between the A and B excitons, where $\Delta E_{\text{Exciton}}$ and A_V/A_0 accelerates for the B exciton compared to the A. The energy difference between the A and B excitons is plotted in the inset of Figure 3b. The maximum spin-orbit (SO) splitting energy measured here is 170 meV at 1.6 V, consistent with previous reports;[46] however at the most negative potentials, the difference reduces to ~130 meV. In the limit of the pure Burstein-Moss conduction band-filling model in a confined system, A_V/A_0 and $\Delta E_{\text{Exciton}}$ are expected to be indistinguishable for both A and B excitons as the SO splitting originates in the valence band and carrier injection only populates the conduction band. This divergence, therefore, suggests that the electrochemical bias or introduction of carriers modifies the nature of the MoS_2 SO transition, and may be an optical signature of reduced vdW interaction between layers; a possible sign of mechanical deformation.[53]

To inspect the reversibility of these spectral changes, we plot the same specroelectrochemical data scanning from negative to positive potentials (reverse direction) plotted as triangles in Figure 3b for the A exciton. At potentials < 0 V, the reverse traces display a slight hysteresis compared to the forward scan, where $\Delta E_{\text{Exciton}}$ and A_V/A_0 are shifted positive in potential compared to the forward scan by ~0.5 V. However, at potentials ≥ 0 V, $\Delta E_{\text{Exciton}}$ and A_V/A_0 converge to the forward scan confirming that these changes are fully reversible. The B exciton displays a similar trend (Figure S7). Electrolyte cation size has been shown to affect the spectroelectrochemical response of colloidal quantum dot thin films;[54] however, when smaller Li^+ cations are used as the supporting electrolyte instead of $[Bu_4N]^+$, no changes in $\Delta E_{\text{Exciton}}$ and A_V/A_0 are observed within the error of the measurement (Supporting Information Figure S8). This control experiment indicates that the cation identity is unimportant in determining the MoS_2 spectra and suggests that the hysteresis is related to MoS_2 and not the structure of the thin film. Determining the origin of the scan direction asymmetry is an intriguing question that will be pursued in future work.

Both electronic doping and electric field effects have been shown to modify the MoS_2 structure.[39, 40, 55, 56] We therefore hypothesize that structural modifications are indeed be present under these *in-situ* conditions. Raman modes are particularly sensitive to specific strain types; thus, we perform *in-situ* Raman spectroscopy on $< N > = 3$ ML MoS_2. The spectra, in 0.5 V intervals, are shown in Figure 4a. At the most positive potential, 1.5 V, two peaks are present within the spectroscopic window: the doubly degenerate, in-plane E_{2g} mode and singly degenerate, out-of-plane A_{1g} mode.[57-59] As the potential is swept from positive to negative, the A_{1g} mode begins to lose intensity and shift to lower frequencies until it nearly merges with the E_{2g} mode. The E_{2g} mode displays a slight shift (< 1 cm^{-1}) at the most negative potentials but retains its intensity. The width of the E_{2g} peak broadens continuously with negative bias. Following the negative scan direction, the electrode bias is switched to 1.5V (bottom trace). The A_{1g} mode regains intensity, and the E_{2g} mode narrows indicating these electrochemical changes are reversible. To further detail the observed changes in the Raman modes, the A_{1g} and E_{2g} peaks are fit with Lorentzian functions and the data from those fits are shown in Figure 4b.

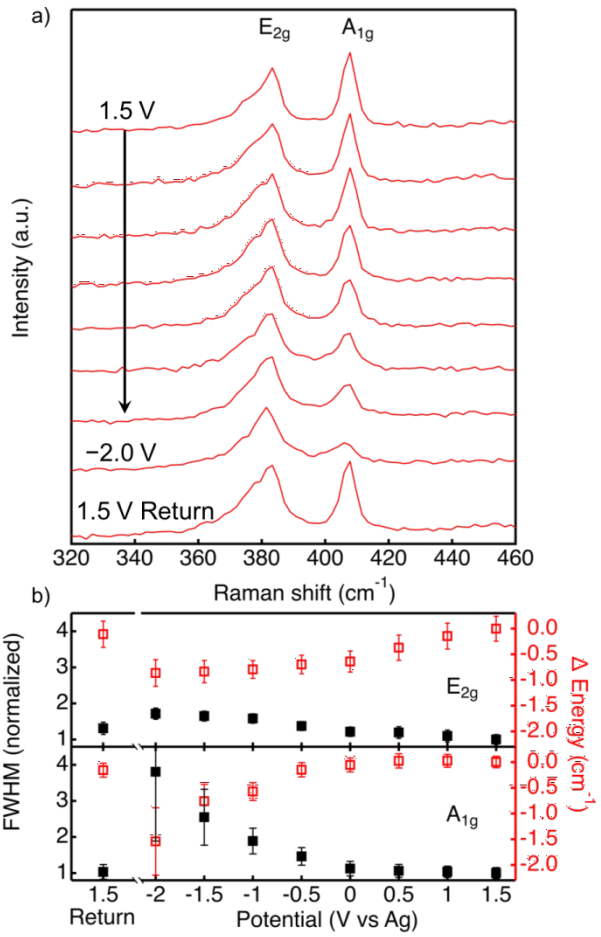

Figure 4. (a) Spectroelectrochemical data for the E_{2g} and A_{1g} Raman modes of $< N > = 3$ ML MoS_2 in dry, anaerobic 0.1 M $[Bu_4N][PF_6]$ acetonitrile electrolyte under varied electrochemical bias. The spectra have been offset vertically for clarity. **(b)** Plots the normalized full-width-at-half-maximum (FWHM), and the shift in peak energy, Δ Energy (red, open shapes) for the A_{1g} (circles) and E_{2g} (squares) Raman modes as a function of applied potential. The FWHM is normalized to the value at 1.5 V. The data are acquired by fitting the Raman spectra with two Lorentzian functions, and the error bars indicate the error from the fit.

From the scatter plots of the fit parameters presented in Figure 4b, the potential onset for the low energy shift and intensity loss of the A_{1g} mode begins near 0.5 V and continues with increasingly negative bias. The attenuation of the A_{1g} mode with negative bias is attributed to an increase in the electron-phonon coupling between A_{1g} and conduction band electrons, which softens and shifts the A_{1g} mode to lower Raman energies.[56] From the A_{1g} total frequency shift, we estimate the carrier density (D_N) at –2 V to be $D_N > 1 \times 10^{13}$ cm^{-2}.[56] The center-of-mass position of the E_{2g} displays a minor negative shift (<1 cm^{-1}) but broadens as the potential is swept negative. We assign this observation to lifting the degeneracy of the E_{2g} mode into an E_{1g}^{+} and E_{1g}^{-} vibration as a result of uniaxial tensile strain induced by electrochemical doping or electric field effects. E_{2g} splitting is unique to uniaxial strain as the symmetry in the *xy* MoS_2 plane is broken.[60-63]

In the single ML limit, optical band gap shifts from increased donor density arise from several competing many-body effects: reduced exciton binding energy, quasi-particle formation, bandgap renormalization, and other coulomb interactions.[26, 30, 31, 64] Extended to several vdW-bound monolayers, however, the effect of a perpendicular electric field on the optical band gap is

quite different. Often referred to as the "Giant Stark Effect", additional vdW-bound MoS_2 layers facilitate electron density polarization in the field direction, which induces a potential energy interlayer anisotropy. The band gap energy decreases linearly with electric field, and eventually transitions from semiconducting (2H) to a metallic (1T) phase.[33-38, 53] The polarizability of 2H-MoS_2 at a given electric field is proportional to the number of vdW-bound layers, where increasing layers reduces the necessary fields for band gap reduction. We therefore carried out the same spectroelectrochemical experiment on $< N >$ = 1.5, 3, and 10 ML MoS_2 samples. The results are summarized in Figure 5.

From Figure 5a, the same general trends in $\Delta E_{Exciton}$ and A_V/A_0 for the A exciton persist for the three different MoS_2 dimensions measured here; as the potential is swept cathodically, $\Delta E_{Exciton}$ red-shifts and A_V/A_0 decreases. However, the magnitude of $\Delta E_{Exciton}$ and A_V/A_0 for a given potential depends on the MoS_2 flake dimensions. The largest changes occur for the highest number of vdW-bound MoS_2 layers, $< N >$ = 10 ML. Between –0.3 V and –1.5 V, the slope of $\Delta E_{Exciton}$ ($\partial \Delta E_{Exciton}\ \partial V^{-1}$) is 38 meV V^{-1} shifting in total 58 meV, and A_V/A_0 almost disappears with a slope ($\partial [A_V/A_0]\ \partial V^{-1}$) of –0.39 V^{-1} and a final value of 0.2. In contrast, $\partial \Delta E_{Exciton}\ \partial V^{-1}$ = 1.5 meV V^{-1} for $< N >$ = 1.5 ML shifting in total ~3.5 meV and $\partial [A_V/A_0]\ \partial V^{-1}$ is –0.03 V^{-1} giving a final value of 0.8. $\partial \Delta E_{Exciton}\ \partial V^{-1}$ and $\partial [A_V/A_0] \partial V^{-1}$ for the intermediate sized sample, $< N >$ = 3 ML, fall between the two extremes. These dimension-dependent values of $\Delta E_{Exciton}$ follow the expected trends for bandgap reduction from dielectric screening in 2D TMDC's;[14, 16, 21] however, the variable excitonic bleach is not predicted by established theory and we therefore account for this discrepancy in the following section.

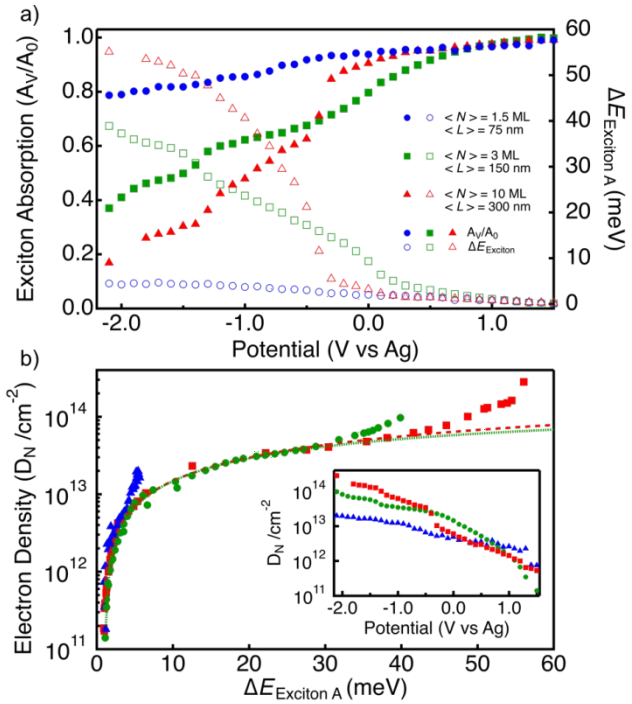

Figure 5. (a) Normalized absorption peak heights, A_V/A_0, (solid shapes) and the peak position shifts, $\Delta E_{Exciton}$, (open shapes) of the A exciton for thin films of $< N >$ = 1.5 ML (blue), 3 ML (green), and 10 ML (red) on FTO as a function of the applied potential in 0.1 M $[Bu_4N][PF_6]$ acetonitrile electrolyte. A_V/A_0 = 1 indicates the potential at which the absorption intensity is the highest, and $\Delta E_{Exciton}$ is the difference in energy (meV) between the absorption peak energy at the maximum and at a given applied potential. Positive values of $\Delta E_{Exciton}$ indicate a red (low energy) shift. **(b)** Plots of $\Delta E_{Exciton}$ against the calculated conduction band electron density (cm^{-2})

with the same color scheme as (a). Fits to $< N >$ = 3 ML (green, dotted) and 10 ML (red dashed) are shown as dashed traces. The inset displays the same electron density data plotted against the applied potential.

Typically, the carrier density (D_N) in a semiconductor conduction band is controlled by the applied potential (V_{App}) according to equation 1:

$$D_N = \int_0^{E_{CB} + kT} N(E;V_{App})(1 - f(E;V_{App}))dE \qquad \text{Equation 1,}$$

where $N(E)$ is the electronic density of states up to energy level E, and $f(E)$ is the Fermi-Dirac distribution function. D_N is therefore proportional to V_{App} through $D_N \propto \exp\left(\frac{V_{App} - E_{CB}}{kT}\right)$ where E_{CB} is the conduction band edge energy. Because MoS_2 is in direct contact with the working electrode and the MoS_2 flakes are sufficiently thin (1 to 10 nm in all cases), V_{App} is a direct measure of MoS_2 E_F (*i.e.* $V_{App} = E_F$). As E_F moves within 1 kT of E_{CB}, D_N is expected to display the same exponential dependence on E_{Vapp} for all thicknesses measured. Since A_V/A_0 is proportional to D_N, A_V/A_0 should also display an exponential dependence on V_{App}. From Figure 5a, this is clearly not the case. Indeed, every flake dimension displays a unique dependence of A_V/A_0 on V_{App} and none display the expected exponential behavior. The effect of electrochemical bias on MoS_2 thus requires further consideration.

We hypothesize that in contrast to traditional semiconductor electrodes, the potentials of the band edges (E_{CB}) are dynamic and depend on V_{App}. In this case, D_N will display the expected conduction band electron population statistics on the dynamic parameter $\Delta E_{\text{Exciton}}$ rather than V_{App} by:

$$D_N = N_C\left(1 - \exp\left[\frac{\chi \bullet \Delta E_{\text{Exciton}}}{kT}\right]\right) \qquad \text{Equation 2,}$$

where N_C is an effective density of states for all states within a few kT above the conduction band edge. Since $\Delta E_{\text{Exciton}}$ is determined optically and is the sum of both the valence and conduction band potential energy shifts, we introduce the unitless parameter χ which is the fraction of the conduction band shift relative the total band gap change (i.e. $\chi = \Delta E_{\text{CB}}/[\Delta E_{\text{CB}} + \Delta E_{\text{VB}}]$).

Figure 5b plots the dependence of D_N on $\Delta E_{\text{Exciton}}$ and displays the same trend for all flake dimensions (D_N is calculated from the absorption spectra, see Supporting Information for details). In the low $\Delta E_{\text{Exciton}}$ regime ($0 < \Delta E_{\text{Exciton}} < 5$ meV), the electron population rises steeply with increasing $\Delta E_{\text{Exciton}}$ indicating that E_F is within the band gap. At $\Delta E_{\text{Exciton}}$ = 5 meV, the slope of D_N flattens with further band gap reduction indicating that E_F is approaching the conduction band edge. For $< N >$ = 1.5, both D_N and $\Delta E_{\text{Exciton}}$ stop at the curves' inflection point. The $< N >$ = 3 ML and 10 ML samples cross the inflection point and continue to reach their respective maxima. All three curves follow the same trajectory until deviation from the exponential trace at their highest D_N values. The divergence is due to a break-down of the assumptions made in calculating D_N (*e.g.*, E_F achieves electronic degeneracy with the conduction band and crosses the Mott transition threshold or the MoS_2 dielectric changes significantly). To emphasize that D_N is not following traditional semiconductor dependence, the same D_N data is plotted against V_{App} in the Figure 5b inset; no MoS_2 samples display the expected exponential dependence. The $< N >$ = 3 ML and 10 ML traces in Figure 5b are fit to equation 2 and are shown as the green dotted and red dashed lines,

respectively. From these fits it is clear that the relationship between D_N and $\Delta E_{\text{Exciton}}$ is independent of flake dimension as either fit is superimposable on the other. The fitted value of kT is 55 ± 11 meV, indicating that $\chi \sim 1/2$ to satisfy the value of kT at room temperature. This implies that the conduction band and valence band shift equally under applied bias. The combination of exponential dependence of D_N on $\Delta E_{\text{Exciton}}$, all three traces aligning with each other, and reproduceable values of kT indicate that electronic doping is dependent on shifting band edge potentials with applied electric field. Therefore, the classical description of the interfacial thermodynamics does not adequately describe few-layer MoS_2.

The relationship between D_N, $\Delta E_{\text{Exciton}}$, and the layer thickness dimension may be understood within the framework of altering the semiconductor band edge potentials. In response to the applied electric field, the MoS_2 band gap decreases, which forces the conduction(valence) band edge potentials to shift in the positive(negative) direction. The MoS_2 E_F equilibrates with the V_{App} by injecting conduction band electrons. Because the magnitude of the band gap shrinkage at a given potential increases with increasing flake thickness, so too does D_N. These results demonstrate that the dielectric screening of the MoS_2 dictates not only the band gap but also the band edge potentials and the donor density under electrochemical bias.

Discussion

The implications of the properties observed above are important with respect to (photo)electrochemical catalysis and the thermodynamics that underpin interfacial charge transfer processes from non-degenerately doped semiconductors. These differences are illustrated schematically in Figure 6. For ideal semiconductors under equilibrium conditions, E_F equilibrates to the redox potential of the solution by distributing majority carriers toward the surface and, consequently, forming a space-charge region causing band bending within the semiconductor. The driving force for spontaneous electron transfer (ΔG_{CT}) across the semiconductor|liquid junction (SCLJ) is governed by the difference between the electrochemical potential of the redox couple ($E^{0/+}$) and the band edge potential at the SCLJ. Application of an electrochemical bias drives E_F away from the equilibrium position, but the potential drops predominantly across the semiconductor. Thus, the band edge potentials at the SCLJ remain pinned, and ΔG_{CT} remains unchanged (Figure 6, left schematic).[23, 65] The exception is when the potential drop occurs within the Helmholtz region which is typically a result of Fermi-level pinning or degenerate doping, not considered here. ΔG_{CT} is therefore independent of applied potential when E_F is within the band gap and depends only on the band edge and redox couple potentials.

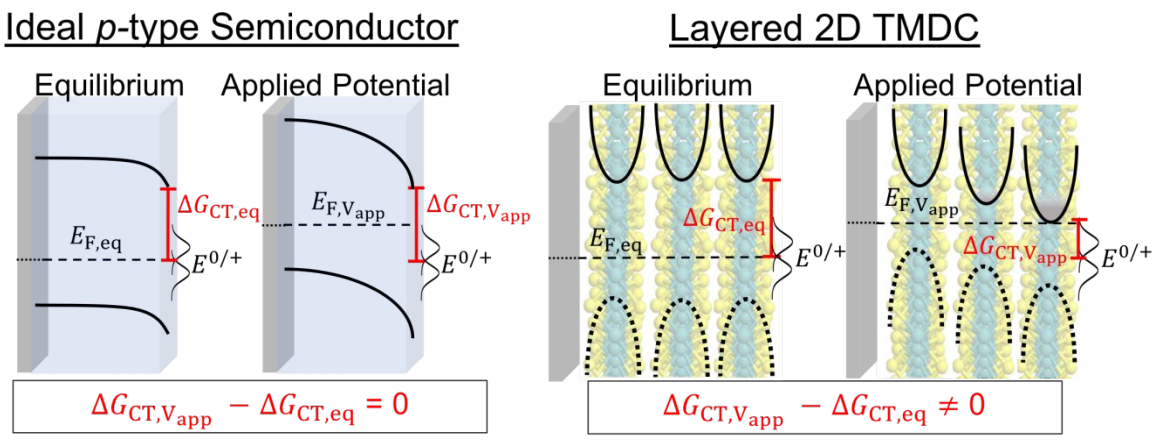

Figure 6. Schematic illustration of (left) traditional semiconductor thermodynamic driving forces for the (photo)electrochemical charge injection under equilibrium and under reverse bias conditions. (Right) The same thermodynamic parameters but adjusted for the dynamic band gap of semiconducting 2D materials. Importantly, this scheme depicts semiconductor electrodes under non-equilibrium conditions where interfacial charge transfer is taking place.

The response of 2H-MoS_2 to an electric field produces fundamentally different interfacial energetics. When electron density is polarized in few-layer MoS_2, the band edges of the individual layers become energetically staggered against one another (rather than continuous band bending) as a result of 2D confinement. This effect has been predicted by computational simulations[38, 66] and observed in experiment.[38] Simultaneously, the band gap reduction observed in few-layer MoS_2 pulls the conduction and valence bands together and attenuates ΔG_{CT} compared to equilibrium conditions. The band gap reduction therefore produces band edge potentials that depends on the V_{App}. In other words, the electrode polarization screening from MoS_2 makes the conduction band edge potential and thus ΔG_{CT}, *dynamic* parameters that depend on V_{App}.

To test the relevance of band gap reduction under electrocatalytic conditions, we perform *operando* spectroelectrochemistry under dark HER conditions. Figure 7 shows the cyclic voltammogram (CV) of $< N > = 3$ ML MoS_2 sample in pH 5 aqueous electrolyte where HER is apparent from the steep, irreversible current feature. A_V/A_0 and $\Delta E_{Exciton}$ are shown for the same electrode as the black and red traces, respectively. Comparing A_V/A_0 and $\Delta E_{Exciton}$ against the CV trace, the onset for both A_V/A_0 and $\Delta E_{Exciton}$ occur at more positive potentials than HER, indicating that bandgap reduction and carrier injection is inexorably linked to HER catalysis. The magnitude of A_V/A_0 and $\Delta E_{Exciton}$ is reduced compared to the anaerobic organic electrolyte where the maximum $A_V/A_0 = 0.73$ and $\Delta E_{Exciton} = 14$ meV are observed compared to $A_V/A_0 = 0.38$ and $\Delta E_{Exciton} = 38$ meV, but the slopes of these curves are comparable to the anaerobic case where $\partial[A_V/A_0]\,\partial V^{-1} = -0.18\ V^{-1}$ and $\partial \Delta E_{Exciton}\,\partial V^{-1} = 11$ meV V^{-1} for aqueous electrolyte and $\partial[A_V/A_0]\,\partial V^{-1} = -0.16\ V^{-1}$ and $\partial \Delta E_{Exciton}\,\partial V^{-1} = 9.7$ meV V^{-1} for the anaerobic organic electrolyte. Indeed, the voltage-dependent spectroscopic signatures of band edge potential realignment observed under anaerobic conditions occur at the same rate under electrocatalytic conditions, which indicate attenuated interfacial energetics.

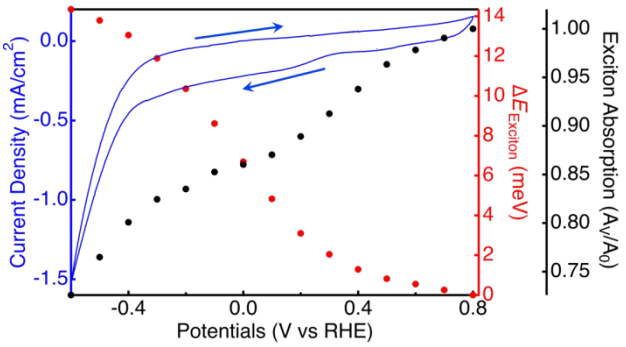

Figure 7. Normalized exciton absorption, A_V/A_0, (black) and peak position shifts, $\Delta E_{Exciton}$, (red) of the A exciton for an MoS_2 thin film with $\langle N_{avg} \rangle$ = 3 ML on FTO as a function of the applied potential in 0.1 M KH_2PO_4 pH 5 aqueous buffer solution. A_V/A_0 = 1 indicates the potential at which the absorption intensity is the highest, and $\Delta E_{Exciton}$ is the difference in energy (meV) between the absorption peak energy at the maximum and at a given applied potential. Positive values of $\Delta E_{Exciton}$ indicate a red (low energy) shift. The blue trace is the cyclic voltammogram of the same MoS_2 electrode where the arrows indicate the scan direction.

The modified interfacial energetics raise intriguing questions about the utility of 2D nanomaterials for photoelectrochemical catalysis. For example, a negative free energy of charge transfer is required to spontaneously drive fuel-forming reactions, but anything more than the thermodynamic minimum plus small kinetic overpotentials is wasted energy and dissipated by heat. In MoS_2, the field-induced band gap reduction observed here is a way to reduce the wasted energy upon electron transfer and provide an additional benefit of simultaneously increasing light absorption. Furthermore, since the rate constant of electron transfer (k_{CT}) is proportional to the difference between the semiconductor band edge potential and the substrate redox potential (*i.e.*, $k_{CT} \propto \exp \frac{\Delta G_{CT}}{kT}$), the applied electrochemical potential will affect k_{CT} in MoS_2 in a manner not observed in traditional Gerischer-like semiconductor photoelectrodes. Indeed a similar effect has been demonstrated before on monolayer MoS_2 in an electric-field effect gated configuration where the gate voltage shifts the band energies of the monolayer MoS_2.[67] Designing dynamic photoelectrode interfaces featuring this phenomenon could thus prove useful for energy conversion optimization in heterogeneous photoelectrocatalysis.

Conclusion

We study the interfacial energetics of 2H-MoS_2 by probing the changes to its electronic structure as a function of applied potential using *in-situ* spectroelectrochemical measurements. We show that electron injection into the conduction band is coupled with a low energy shift of the exciton resonance, both properties depending on the number of MoS_2 layers in the vertical dimensions. In addition, the applied electric field/electronic doping imparts a structural change as indicated by broadening Raman signals. In contrast to conventional semiconductors, we show that conduction band electron injection is dependent on the change in the excitonic energy and not just the applied potential. This observation indicates that the relevant semiconductor|liquid interfacial energetics change with varied electric fields, a property not observed in typical semiconductors. We demonstrate that the spectroscopic signatures of band gap reduction and carrier injection occur under photoelectrocatalytic hydrogen evolution conditions. The results presented herein highlight the possibility of using 2D transition metal dichalcogenides more effectively to improve energy conversion efficiencies over traditional semiconductors. The voltage-dependent interfacial

energetics from TMDC electrodes reported here is a new and potentially interesting avenue to explore for heterogeneous (photo)electrocatalysis.

Acknowledgments
This work was conducted by all co-authors, employees of the Alliance for Sustainable Energy, LLC, the manager and operator of the National Renewable Energy Laboratory for the U.S. Department of Energy (DOE) under Contract No. DE-AC36-08GO28308. Funding provided by the U.S. DOE, Office of Science, Office of Basic Energy Sciences, Division of Chemical Sciences, Geosciences, and Biosciences, Solar Photochemistry Program.

References

1. E. E. Benson, H. Zhang, S. A. Schuman, S. U. Nanayakkara, N. D. Bronstein, S. Ferrere, J. L. Blackburn and E. M. Miller, *J. Am. Chem. Soc.*, 2018, **140**, 441-450.
2. A. Vilan and D. Cahen, *Chem. Rev.*, 2017, **117**, 4624-4666.
3. J. Deng, H. Li, J. Xiao, Y. Tu, D. Deng, H. Yang, H. Tian, J. Li, P. Ren and X. Bao, *Energy Environ. Sci.*, 2015, **8**, 1594-1601.
4. H. Li, J. Li, Z. Ai, F. Jia and L. Zhang, *Angew. Chem., Int. Ed.*, 2018, **57**, 122-138.
5. R. Liu, Z. Zheng, J. Spurgeon and X. Yang, *Energy Environ. Sci.*, 2014, **7**, 2504-2517.
6. R. van de Krol, *Photoelectrochemical Hydrogen Production*, Springer US, 1 edn., 2012.
7. H. Li, C. Tsai, A. L. Koh, L. Cai, A. W. Contryman, A. H. Fragapane, J. Zhao, H. S. Han, H. C. Manoharan, F. Abild-Pedersen, J. K. Nørskov and X. Zheng, *Nat. Mater.*, 2015, **15**, 48.
8. D. Voiry, H. Yamaguchi, J. Li, R. Silva, D. C. B. Alves, T. Fujita, M. Chen, T. Asefa, V. B. Shenoy, G. Eda and M. Chhowalla, *Nat. Mater.*, 2013, **12**, 850.
9. H. Jin, C. Guo, X. Liu, J. Liu, A. Vasileff, Y. Jiao, Y. Zheng and S.-Z. Qiao, *Chem. Rev.*, 2018, **118**, 6337-6408.
10. T. F. Jaramillo, K. P. Jørgensen, J. Bonde, J. H. Nielsen, S. Horch and I. Chorkendorff, *Science*, 2007, **317**, 100-102.
11. D. Deng, K. S. Novoselov, Q. Fu, N. Zheng, Z. Tian and X. Bao, *Nat. Nanotechnol.*, 2016, **11**, 218.
12. J. Gu, J. A. Aguiar, S. Ferrere, K. X. Steirer, Y. Yan, C. Xiao, James L. Young, M. Al-Jassim, N. R. Neale and J. A. Turner, *Nature Energy*, 2017, **2**, 16192.
13. X. Yu and K. Sivula, *Curr. Opin. Electrochem.*, 2017, **2**, 97-103.
14. J. Xie, J. Zhang, S. Li, F. Grote, X. Zhang, H. Zhang, R. Wang, Y. Lei, B. Pan and Y. Xie, *J. Am. Chem. Soc.*, 2013, **135**, 17881-17888.
15. S. Jayabal, G. Saranya, J. Wu, Y. Liu, D. Geng and X. Meng, *Journal of Materials Chemistry A*, 2017, **5**, 24540-24563.
16. W. Kautek and H. Gerischer, *Berichte der Bunsengesellschaft für physikalische Chemie*, 1980, **84**, 645-653.
17. G. Djemal, N. Müller, U. Lachish and D. Cahen, *Sol. Energy Mater.*, 1981, **5**, 403-416.
18. X. Yu and K. Sivula, *Chem. Mater.*, 2017, **29**, 6863-6875.

19. X. Yu, N. Guijarro, M. Johnson and K. Sivula, *Nano Lett.*, 2018, **18**, 215-222.
20. M. Velický, M. A. Bissett, C. R. Woods, P. S. Toth, T. Georgiou, I. A. Kinloch, K. S. Novoselov and R. A. W. Dryfe, *Nano Lett.*, 2016, **16**, 2023-2032.
21. M. Faraji, M. Yousefi, S. Yousefzadeh, M. Zirak, N. Naseri, T. H. Jeon, W. Choi and A. Z. Moshfegh, *Energy Environ. Sci.*, 2019, DOI: 10.1039/C8EE00886H.
22. X. Yang and D. Wang, *ACS Appl. Energy Mater.*, 2018, DOI: 10.1021/acsaem.8b01345.
23. R. Memming, *Semiconductor Electrochemistry*, WILEY-VCH, 2007.
24. Y. Yu, S.-Y. Huang, Y. Li, S. N. Steinmann, W. Yang and L. Cao, *Nano Lett.*, 2014, **14**, 553-558.
25. Q. H. Wang, K. Kalantar-Zadeh, A. Kis, J. N. Coleman and M. S. Strano, *Nat. Nanotechnol.*, 2012, **7**, 699.
26. K. Yao, A. Yan, S. Kahn, A. Suslu, Y. Liang, E. S. Barnard, S. Tongay, A. Zettl, N. J. Borys and P. J. Schuck, *Phys. Rev. Lett.*, 2017, **119**, 087401.
27. B. Liu, W. Zhao, Z. Ding, I. Verzhbitskiy, L. Li, J. Lu, J. Chen, G. Eda and K. P. Loh, *Adv. Mater.*, 2016, **28**, 6457-6464.
28. A. Chernikov, A. M. van der Zande, H. M. Hill, A. F. Rigosi, A. Velauthapillai, J. Hone and T. F. Heinz, *Phys. Rev. Lett.*, 2015, **115**, 126802.
29. Y. Liang and L. Yang, *Phys. Rev. Lett.*, 2015, **114**, 063001.
30. D. K. Efimkin and A. H. MacDonald, *Phys. Rev. B*, 2017, **95**, 035417.
31. K. F. Mak, K. He, C. Lee, G. H. Lee, J. Hone, T. F. Heinz and J. Shan, *Nat. Mater.*, 2012, **12**, 207.
32. C. Cui, F. Xue, W.-J. Hu and L.-J. Li, *npj 2D Mater. and Appl.*, 2018, **2**, 18.
33. X. Lu and L. Yang, *Appl. Phys. Lett.*, 2017, **111**, 193104.
34. Y. Qu, C. Shengli, K. Jun, Z. Xueao, S. Zhengzheng, Q. Shiqiao and L. Jingbo, *J. Phys.: Condens. Matter*, 2012, **24**, 335501.
35. Q. Liu, L. Li, Y. Li, Z. Gao, Z. Chen and J. Lu, *J. Phys. Chem. C*, 2012, **116**, 21556-21562.
36. A. Kuc and T. Heine, *Chem. Soc. Rev.*, 2015, **44**, 2603-2614.
37. A. Ramasubramaniam, D. Naveh and E. Towe, *Phys. Rev. B*, 2011, **84**, 205325.
38. M. Kang, B. Kim, S. H. Ryu, S. W. Jung, J. Kim, L. Moreschini, C. Jozwiak, E. Rotenberg, A. Bostwick and K. S. Kim, *Nano Lett.*, 2017, **17**, 1610-1615.
39. W. Wu, L. Wang, Y. Li, F. Zhang, L. Lin, S. Niu, D. Chenet, X. Zhang, Y. Hao, T. F. Heinz, J. Hone and Z. L. Wang, *Nature*, 2014, **514**, 470.
40. C. J. Brennan, R. Ghosh, K. Koul, S. K. Banerjee, N. Lu and E. T. Yu, *Nano Lett.*, 2017, **17**, 5464-5471.
41. A. Walsh, J. L. F. Da Silva and S.-H. Wei, *Phys. Rev. B*, 2008, **78**, 075211.
42. A. M. Schimpf, K. E. Knowles, G. M. Carroll and D. R. Gamelin, *Acc. Chem. Res.*, 2015, **48**, 1929-1937.
43. A. Splendiani, L. Sun, Y. Zhang, T. Li, J. Kim, C.-Y. Chim, G. Galli and F. Wang, *Nano Lett.*, 2010, **10**, 1271-1275.
44. K. F. Mak, C. Lee, J. Hone, J. Shan and T. F. Heinz, *Phys. Rev. Lett.*, 2010, **105**, 136805.
45. R. Ganatra and Q. Zhang, *ACS Nano*, 2014, **8**, 140414122657007.
46. G.-B. Liu, D. Xiao, Y. Yao, X. Xu and W. Yao, *Chem. Soc. Rev.*, 2015, **44**, 2643-2663.
47. C. Backes, R. J. Smith, N. McEvoy, N. C. Berner, D. McCloskey, H. C. Nerl, A. O'Neill, P. J. King, T. Higgins, D. Hanlon, N. Scheuschner, J. Maultzsch, L. Houben, G. S. Duesberg, J. F. Donegan, V. Nicolosi and J. N. Coleman, *Nature Comm.*, 2014, **5**, 4576.

48. C. Backes, B. M. Szydłowska, A. Harvey, S. Yuan, V. Vega-Mayoral, B. R. Davies, P.-l. Zhao, D. Hanlon, E. J. G. Santos, M. I. Katsnelson, W. J. Blau, C. Gadermaier and J. N. Coleman, *ACS Nano*, 2016, **10**, 1589-1601.
49. B. Radisavljevic, A. Radenovic, J. Brivio, V. Giacometti and A. Kis, *Nat. Nanotechnol.*, 2011, **6**, 147.
50. E. A. A. Pogna, M. Marsili, D. De Fazio, S. Dal Conte, C. Manzoni, D. Sangalli, D. Yoon, A. Lombardo, A. C. Ferrari, A. Marini, G. Cerullo and D. Prezzi, *ACS Nano*, 2016, **10**, 1182-1188.
51. J. R. Dunklin, H. Zhang, Y. Yang, J. Liu and J. van de Lagemaat, *ACS Energy Lett.*, 2018, **3**, 2223-2229.
52. D. Tsokkou, X. Yu, K. Sivula and N. Banerji, *J. Phys. Chem. C*, 2016, **120**, 23286-23292.
53. E. J. G. Santos and E. Kaxiras, *ACS Nano*, 2013, **7**, 10741-10746.
54. S. C. Boehme, H. Wang, L. D. A. Siebbeles, D. Vanmaekelbergh and A. J. Houtepen, *ACS Nano*, 2013, **7**, 2500-2508.
55. K.-A. N. Duerloo, M. T. Ong and E. J. Reed, *J. Phys. Chem. Lett.*, 2012, **3**, 2871-2876.
56. B. Chakraborty, A. Bera, D. V. S. Muthu, S. Bhowmick, U. V. Waghmare and A. K. Sood, *Phys. Rev. B*, 2012, **85**, 161403.
57. H. J. Conley, B. Wang, J. I. Ziegler, R. F. Haglund, S. T. Pantelides and K. I. Bolotin, *Nano Lett.*, 2013, **13**, 3626-3630.
58. L. Hong, Z. Qing, Y. C. C. Ray, T. B. Kang, E. T. H. Tong, O. Aurelien and B. Dominique, *Adv. Funct. Mater.*, 2012, **22**, 1385-1390.
59. C. Lee, H. Yan, L. E. Brus, T. F. Heinz, J. Hone and S. Ryu, *ACS Nano*, 2010, **4**, 2695-2700.
60. W. Yanlong, C. Chunxiao, Q. Caiyu and Y. Ting, *Small*, 2013, **9**, 2857-2861.
61. W. Wu, J. Wang, P. Ercius, N. C. Wright, D. M. Leppert-Simenauer, R. A. Burke, M. Dubey, A. M. Dogare and M. T. Pettes, *Nano Lett.*, 2018, **18**, 2351-2357.
62. X. Zhang, X.-F. Qiao, W. Shi, J.-B. Wu, D.-S. Jiang and P.-H. Tan, *Chem. Soc. Rev.*, 2015, **44**, 2757-2785.
63. C.-H. Chang, X. Fan, S.-H. Lin and J.-L. Kuo, *Phys. Rev. B*, 2013, **88**, 195420.
64. T. C. Berkelbach, M. S. Hybertsen and D. R. Reichman, *Phys. Rev. B*, 2013, **88**, 045318.
65. A. J. Bard and M. Stratmann, *Encyclopedia of Electrochemistry: Semiconductor electrodes and photoelectrochemistry*, Wiley-VCH.
66. T. Brumme, M. Calandra and F. Mauri, *Phys. Rev. B*, 2015, **91**, 155436.
67. Y. Wang, C.-H. Kim, Y. Yoo, J. E. Johns and C. D. Frisbie, *Nano Lett.*, 2017, **17**, 7586-7592.

Carroll et al.
April 1, 2019

TOC GRAPHIC

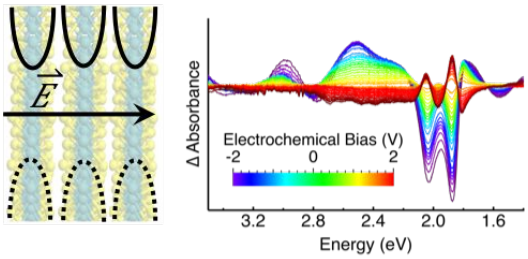

In-situ and *operando* spectroelectrochemistry are used to study the interfacial thermodynamics of few-layer MoS_2 for (photo)electrocatalysis.